Mon. Not. R. Astron. Soc. **000**, 1–5 (2018) Printed 10 September 2018 (MN LATEX style file v2.2)

Two Super-Earths in the 3:2 MMR around KOI-1599?

F. Panichi[1] & K. Goździewski[2]
[1]*Institute of Physics and CASA*, Faculty of Mathematics and Physics, University of Szczecin, Wielkopolska 15, 70-451 Szczecin, Poland*
[2]*Centre for Astronomy, Faculty of Physics, Astronomy and Informatics, Nicolaus Copernicus University, Grudziadzka 5, 87-100 Toruń, Poland*

Accepted .... Received ...; in original form ...

ABSTRACT
We validate the planetary origin of the KOI-1599 transit time variations (TTVs) with statistical and dynamical tests. The observed TTVs are strongly anti-correlated, suggestive of two mutually interacting planets. They have the same radii, 1.9 ± 0.2 $R_\oplus$ (the inner KOI-1599.02), and $1.9 \pm 0.3 R_\oplus$ (the outer KOI-1599.01). The TTVs make it possible to constrain the planet masses safely below dynamical instability limit of $\simeq 3$ m_{Jup}, to (9.0 ± 0.3) $m_\oplus$, and (4.6 ± 0.3) $m_\oplus$, for the inner and the outer planet, respectively, at low-eccentric ($e \simeq 0.01$) orbits. In such a case, the planets are trapped in the 3:2 mean motion resonance with anti-aligned apsides ($\Delta\varpi = \pi$), consistently with a likely migration history of the system.

Key words: celestial mechanics – planetary systems – stars: individual: KOI-1599

1 INTRODUCTION

The KEPLER mission (Borucki et al. 2011) discovered hundreds of extra-solar multiple planetary systems (`https://exoplanetarchive.ipac.caltech.edu/`). The distribution of the period-ratio in the KEPLER sample (Lissauer et al. 2011; Fabrycky et al. 2014; Delisle & Laskar 2014) shows a paucity of systems near to first-order MMRs, with a significant peak close to the 3:2 mean motion resonance (MMR). Such features of the period-ratio distribution may be related to the formation history and dynamic evolution of multiple planet systems (e.g., Lithwick & Wu 2012; Batygin & Morbidelli 2013; Papaloizou 2015). It is therefore critical to determine whether a multiple planetary system is dynamically resonant or only close to a strictly resonant configuration (e.g., Goldreich & Schlichting 2014).

A crucial data source regarding the multiple KEPLER planet configurations are the TTV measurements, listed in recent catalogues by Rowe et al. (2015) and Holczer et al. (2016) (furthermore, H16). The data span the Q1-Q16 quarters of the KEPLER light-curves (LCs). Through inspecting these measurements, we selected KOI-1599 with two putative planetary companions, with the inner candidate marked as a possible planet and the outer one not yet examined in the NASA Exoplanet Archive. The TTVs of KOI-1599 exhibit an anti-correlated sinusoidal trend, indicative of two gravitationally interacting objects (e.g., Steffen et al. 2012; Steffen & Hwang 2015). Our primary motivation for investigating this putative 2-planet configuration is the proximity of their orbital periods to the 3:2 MMR. We did not find any studies aiming to validate and characterise this interesting and likely resonant system.

Since the star is dim ($V \simeq 15$ mag), it would be a difficult target for a spectroscopic follow-up, and we aim to constrain masses of the planetary companions with the TTV orbital model (e.g. Agol et al. 2005; Holman et al. 2010). Recently, Baranec et al. (2016) imaged ~ 1000 dim KEPLER stars unsuitable for the spectroscopic follow-up. They detected two nearby dim field stars, yet with a substantial angular separation of ~ 3 arcsec from KOI-1599, which may dismiss the blend effect. We aim to verify this furthermore on the dynamical grounds, re-compute the planet-to-star radius-ratio, and the density estimates for the candidate planets.

In this work, we follow Holman et al. (2010); Nesvorný et al. (2013); MacDonald et al. (2016), as well as Panichi et al. (2018), regarding the dynamical photometry method. In Sect. 2, we re-analysed the whole Q1-Q17 DR-25 KEPLER LCs of KOI-1599, and we update the TTVs measurements. In Sect. 3, we validated the two transiting objects as planets. In Sect. 4, the orbital model and masses of the 2-planet configuration are derived. In Sect. 5, the 3:2 MMR resonant architecture is characterised. Internal compositions of the planets are discussed in Sect. 6, and conclusions are in Sect. 7. Supplementary Material (SM) is presented on-line.

2 THE LIGHT-CURVE ANALYSIS AND TTVS

Aiming to validate the KOI-1599 planets, we used the KEPLER photometric data only. We re-analysed the corrected, de-trended LC-INIT light-curves (LCs) from the DR-25 KEPLER release, spanning the whole Q1-Q17 quarters, also in order to verify and, possibly, refine the previous TTVs measurements. To avoid confusion, the inner planet KOI-1599.02 has index "1" and the outer planet KOI-1599.01 is labeled with "2", respectively. With the box-least-squares (BLS) algorithm (Kovács et al. 2002), we searched for periodic signals in the LCs. The two transiting objects are apparently close to the 3:2 MMR, thus their mid-transit times may be significantly shifted from the linear ephemeris.

We extracted the TTVs from the LC-INIT LCs following Panichi et al. (2018). The LCs were split in fragments and we se-

lected a narrow window (± 0.5 days) at multiples of the two periods obtained with the BLS search. Each of them should contain only one transit-like signature. Once the out-of-transit parts of each fragments were re-normalised, they were superimposed in order to obtain a folded LC for both planets. The EXONAILER package of Espinoza et al. (2016) was used for preliminary estimations of the planet-to-star radius-ratio (p) and the orbital inclination (I). The quadratic limb-darkening coefficients were interpolated, based on data in the NASA archive. The photometric noise σ_w was kept fixed and estimated from the off-transit fragments of the LCs. After fixing these parameters, we fitted for each of the LC fragments the related mid-transit moment (T). This preliminary list of mid-transit times was applied for re-folding each of the fragments, and the same procedure was iterated until no significant differences in the best-fitting parameters are present. In this way, we controlled the derived TTVs, radii R_i, (1.9 ± 0.2) and (1.9 ± 0.3) Earth radii, as well as orbital inclinations I_i. The system appears as almost coplanar, since the inner planet has $I_1 = 88.60 \pm 0.06$ [deg], while for the outer planet $I_2 = 89.78 \pm 0.1$ [deg].

The median values of the photometric parameters and their uncertainties were derived with the Markov Chain Monte Carlo (MCMC) affine sampler, developed in the EMCEE package by Foreman-Mackey et al. (2013). The resulting parameters and TTV measurements are reported in the SM on-line.

3 VALIDATION OF THE PLANETARY TTV ORIGIN

We applied tests originally proposed by the KEPLER team to validate the majority of candidate planets in multiple systems (e.g. Lissauer et al. 2011; Steffen et al. 2012; Rowe et al. 2014).

The anti-correlation (cross-correlation) of the TTVs can be used to confirm that two objects orbit the same star (Steffen et al. 2012) and their observed anti-correlated TTV signals cannot be a random noise. This method relies on the Monte Carlo bootstrap analysis. A sinusoidal signal with a fixed modulation period is fitted to the TTV series of each planet with the Levenberg-Marquardt algorithm (Press et al. 1986). For each of the sampled periods, the cross-correlation statistic Ξ (Steffen et al. 2012) measures the fit quality — the larger Ξ, the better quality. Figure 1 shows Ξ for the KOI-1599 TTV signals, as a function of the modulation period. Our new TTVs dataset exhibits a peak at a position similar to that one in the H16 data, but it seems to have even larger significance.

The next step consists of the Monte Carlo bootstrap analysis (e.g., Press et al. 1986). We tested 5×10^4 synthetic TTV datasets obtained by random shuffling of the original TTVs, with their uncertainties, and the mid-transit times. As for the real TTV data, each of the randomly generated datasets is fitted with the sine function, and the maximum value of its Ξ is recorded. The results are illustrated in Fig. 1 (middle panel). The False Alarm Probability (FAP) is defined as the ratio of synthetic systems with Ξ larger than that of the observed system to the total number of samples (here, 5×10^4). The histogram indicates that unlikely the sinusoidal TTVs are artefacts. The FAP is smaller than 10^{-3} adopted by Steffen et al. (2012) for validating other KEPLER Objects of Interest (KOIs). We conclude that the KOI-1599 data pass the TTV anti-correlation test.

As a second validation test, we used the dynamical stability constraints. We note that this experiment was not based on the TTVs measurements, rather than on canonical information regarding the orbital periods of transiting objects inferred from the LCs.

In order to conduct the test, the masses, m_1 and m_2, of the two putative transiting objects are changed in a 2-dim grid of 512×512 points. At each point, we constructed a number of synthetic configurations, by fixing their orbital periods (and semi-major axes) in accordance with the mean photometric periods. The mean anomalies and arguments of periastrons are random in the $[0, 2\pi]$ range, as well as the eccentricities are randomly sampled from $[0, 0.1]$. In order to check the stability of these synthetic systems, we used the Lyapunov-based fast indicator MEGNO (Cincotta & Simó 2000; Goździewski et al. 2008).

The results are presented in Fig. 1 for the probability of picking up a stable system in the (m_1,m_2)-plane, for 100 sampled configurations with a fixed pair of masses. Clearly, stable systems are possible unless the masses are larger than 2–3 m_{Jup}. Beyond this limit, the probability of guessing a stable configuration sharply decreases. Moreover, the masses in stable systems are well below the planetary threshold of ~ 14 m_{Jup} (e.g., Spiegel et al. 2011).

4 THE BEST-FITTING TTV MODELS

We applied the same orbital model and the TTV optimisation as in our earlier papers (e.g. Goździewski et al. 2016). We assumed a coplanar system, and the model parameters contains $\boldsymbol{p} = \{m_i, P_i, x_i \equiv e_i \cos\varpi_i, y_i \equiv e_i \sin\varpi_i, T_i\}$ for $i = 1, 2$, where P_i, e_i, ϖ_i and T_i stand for the orbital period, eccentricity, longitude of pericenter and the moment of the first transit, respectively, w.r.t. the initial epoch of $T_0 = \mathrm{BJKD} - 139$ d. We performed a preliminary optimisation of the likelihood function $\mathcal{L}(\boldsymbol{p})$ with the evolutionary algorithms (GEA), but, as anticipated, we could not constrain the eccentricities due to the mass-eccentricity degeneration (e.g., Hadden & Lithwick 2014; Deck & Agol 2015; Jontof-Hutter et al. 2016).

However, having the best-fitting solutions found with GEA, we used the MCMC sampling for characterising these solutions. We set Gaussian priors $\mathcal{N}(\mu, \sigma)$ for the (x_i, y_i)-variables with $\mu_i = 0$ and the same σ_{x_i,y_i} for both planets. In order to asses the proper eccentricity priors σ_{x_i,y_i}, we performed the MCMC sampling for $\sigma_{x_i,y_i} \in [0.001, 0.12]$, with small steps, following a similar strategy as in Migaszewski & Goździewski (2018). The priors were set uniform for all other parameters. We iterated 1024 `emcee` walkers around selected GEA models for up to 256,000 samples each, aiming to keep the acceptance rate between 0.2 and 0.5.

In Fig. 2, posterior distributions are shown in the (m_1, m_2)- and $(\varpi_2, \Delta\varpi)$-plane, $\Delta\varpi \equiv \varpi_2 - \varpi_1$, for two representative $\sigma_{x_i,y_i} = 0.0066$ and 0.12, respectively. For eccentricity priors smaller than the critical one, $\sigma^C_{x_i,y_i} \simeq 0.03$ (tentatively), the posterior is single-modal (the left column of Fig. 2), with $\Delta\varpi \simeq \pi$. We found the posterior more and more asymmetric in $\Delta\varpi$ for $\sigma_{x_i,y_i} > \sigma^C_{x_i,y_i}$, and with two clear local extrema, $\Delta\varpi \simeq \pi, 0$ for $\sigma_{x_i,y_i} > 0.06$. Close to $\sigma^C_{x_i,y_i}$, the $\Delta\varpi = \pi$ mode bifurcates, and a second mode $\Delta\varpi = 0$ (aligned orbits) emerges. An example for $\sigma_{x_i,y_i} = 0.12$ is shown in Fig. 2 (middle column). As the best-fitting TTV model, we report a low-eccentric ($e_i \simeq 0.01$), $\Delta\varpi = \pi$ solution for $\sigma_{x_i,y_i} = 0.0033$ (Tab. 1, Fig. 3). It yields similarly small $\chi^2_\nu \simeq 1.1$ as the best GEA models, $\chi^2_\nu \sim 1$, close to a local minimum, when compared with models for $\sigma_{x_i,y_i} = 0.001$ ($\chi^2_\nu = 1.22$) and $\sigma_{x_i,y_i} = 0.0066$ ($\chi^2_\nu = 1.27$).

Plots in the right column of Fig. 2 illustrate the median values of eccentricities and masses derived from the posterior samples, for a number of runs with $\sigma_{x_i,y_i} \in [0.001, 0.012]$. There is a strong correlation of the median eccentricity with the priors, while mass estimates seem to be clustered, yet in two different regions, relative to $\sigma^C_{x_i,y_i} \simeq 0.03$. Beyond that value, (x_i, x_j) and/or (y_i, y_j) are correlated, and $\Delta\varpi = \pi, 0$ modes appear clearly for $\sigma_{x_i,y_i} > 0.06$, a value likely dependent on the MCMC sampling strategy.

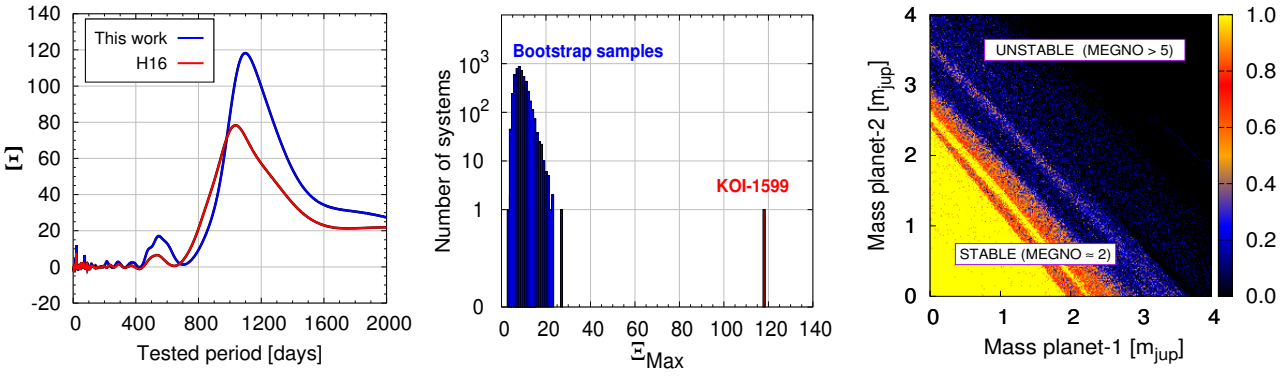

Figure 1. *Left*: Cross-correlation in terms of the Ξ statistics, for our new TTV data (blue line) and H16 dataset (red line), respectively. The modulation period's peak of $\simeq 1100$ d exceeds other peaks. *Middle*: Monte Carlo bootstrap analysis of KOI-1599. The maximum of Ξ for the observed system (red) is much larger than for any of the synthetic configurations (blue). *Right*: the probability of stable systems in the (m_1, m_2)-plane. See the text for details.

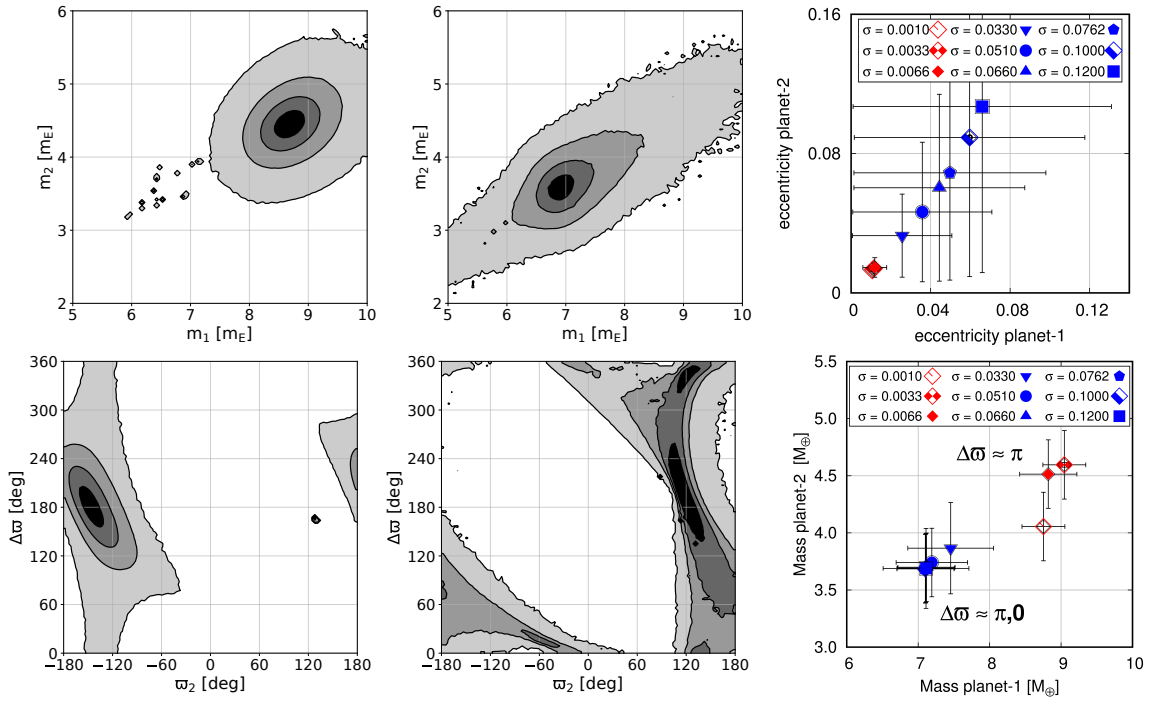

Figure 2. Two-dimensional projections of the MCMC-derived posterior: the left column is for the (m_1, m_2)- and $(\varpi_2, \Delta\varpi)$-plane, where $\Delta\varpi \equiv \varpi_2 - \varpi_1$, respectively for $\sigma_{x_i,y_i} = 0.0066$, representative of a single $\Delta\varpi = \pi$ mode, and the middle column is for σ_{x_i,y_i}=0.12, with two-modal $\Delta\varpi = \pi, 0$ posterior. Contours illustrate the 14-, 50-, 86- and 99.9-th percentile of the posterior samples. The right column is for the median values of eccentricities and masses derived as medians of the posterior samples, for different eccentricity priors $\sigma \equiv \sigma_{x_i,y_i}$. Their formal uncertainties are marked with cross-hairs. We distinguish between clear single-mode $\Delta\varpi = \pi$ solutions yielding $\chi^2_\nu \simeq 1.1$ (red symbols) and other models with asymmetric or dual-mode posterior in $\Delta\varpi$ (blue symbols).

This experiment shows that it is not possible to distinguish between solutions with these two modes using only the TTV observations. Also, the mass-eccentricity degeneracy (e.g., Hadden & Lithwick 2014; Jontof-Hutter et al. 2016) cannot be fully removed with a "reasonable" selection of the eccentricity priors. The masses and eccentricities are globally weakly constrained, mostly due to the two-modal $\Delta\varpi = 0, \pi$ posterior. Additional constraints, like a particular type of periodic configurations (Migaszewski & Goździewski 2018), or flowing from the migration history of the system, could be helpful for resolving this issue. However, for the mass range of KOI-1599, we could not better constrain the eccentricities through preliminary migration simulations following a model in Papaloizou & Larwood (2000). For reasonable disk decay and migration timescales (τ_a, τ_e), the simulations result in systems with $\Delta\varpi = \pi$, but with eccentricities in relatively wide range, $e_i \in (0, \simeq 0.1)$, consistent with Lee & Peale (2002); Batygin & Morbidelli (2013). (See also the SM on-line).

5 DYNAMICS AND THE 3:2 MMR

Although both the GEA and MCMC-sampling experiments make it not possible to constrain eccentricities without additional assumptions, a striking feature of the TTV models distribution is the majority of systems in the anti-aligned libration mode $\Delta\varpi = \pi$. It is expected as a natural outcome of inward and convergent migration

Table 1. The TTV model parameters and their uncertainties from the MCMC sampling, for eccentricity priors $\sigma_{x_i,y_i} = 0.0033$, resulting in $\Delta\varpi = \pi$ and $\chi^2_\nu \simeq 1.1$. The uncertainties are estimated as the 16-th, and 84-th percentile of the samples. The T_0 epoch is BJKD−139 days. The star mass is $m_\star = 1.02$ m$_\odot$, its radius $R_\star = 0.972$ R$_\odot$ (Rowe et al. 2015). Orbital elements a_i, e_i, ϖ_i and $\mathcal{M}_i$ (the mean anomaly at the epoch) are inferred from the model parameters.

Planet	KOI-1599.02	KOI-1599.01
P [d]	13.6088 ±0.0006	20.4415 ± 0.0013
$e\cos\varpi$	0.007 ± 0.003	-0.009 ± 0.003
$e\sin\varpi$	0.009 ± 0.003	-0.011 ± 0.003
T [d]	74.012 ± 0.006	72.946 ± 0.008
mass m [M$_\oplus$]	9.0 ± 0.3	4.6 ± 0.3
a [au]	0.112293	0.147280
e	0.0114	0.0140
ϖ [deg]	49.951	230.175
$\mathcal{M}$ [deg]	167.660	22.141

of the planets. However, combinations of low—moderate eccentricity and aligned—anti-aligned configurations, which fit the TTV observations are also possible.

All the best-fitting (low χ^2_ν) systems exhibit period ratios close to 3:2. In order to assess whether these systems are dynamically resonant, we performed extensive dynamical tests regarding the four classes of configurations, in terms of the critical angles and dynamical maps. We computed critical angles of the 3:2 MMR, $\phi_{3:2,1} = 2\lambda_1 - 3\lambda_2 + \varpi_1$, and $\phi_{3:2,2} = 2\lambda_1 - 3\lambda_2 + \varpi_2$, where λ_i is the mean longitude, and ϖ_i its longitude of periastron ($i = 1, 2$). An example evolution of these angles, indicating their coherence for the anti-aligned solution in Tab. 1 shows Fig. 3 (left-bottom panel), spanning $\sim 2 \times 10^5$ dynamical (outer) periods.

Besides coherent circulations, as in MCMC model in Tab. 1, we found that in the aligned models only one critical angle may librate, while both angles may librate in the anti-aligned models. Remarkably, this is independent on eccentricities and masses.

However, since the libration of critical angles may not be the decisive factor for identifying the MMR dynamics (e.g., Henrard & Lamaitre 1983), we compute dynamical maps in terms of the proper mean motions n_i, $i = 1, 2$ (fundamental frequencies) and their ratio ($f_2/f_1 := n_2/n_1$) with respect to the 3:2 commensurability. The proper mean motions are derived with the modified Fourier transform (FMFT, Šidlichovský & Nesvorný 1996) of the time series $\{a_i(t)\exp[\mathrm{i}\lambda_i(t)]\}$, where $a_i(t)$ and $\lambda_i(t)$ are the Poincaré (canonical), osculating semi-major axes and the mean longitudes, respectively. Fig. 3 shows a deviation of the proper mean motion ratio relative to the 3:2 MMR value, for the anti-aligned MCMC model (Tab. 1). Such dynamical maps reveal the MMR structure and its separatrix region. The model may be clearly identified as dynamically resonant, in spite of a lack of libration of the critical angles.

Generally, all the best-fitting, low χ^2_ν solutions found in the GEA search and with the MCMC sampling are long-term stable. Similarly to the example above, these models are found inside the separatrices of the 3:2 MMR in dynamical maps computed in terms of the MEGNO indicator (not shown here, see the SM on-line).

6 THE DENSITY DICHOTOMY OF KOI-1599 PLANETS

As found with the photometric analysis of the LCs, the KOI-1599 Super-Earths have very similar radii of $\simeq 1.9$ R$_\oplus$. Surprisingly, our estimates differ from data in Rowe et al. (2015). They report a large, likely incorrect radius ~ 64R$_\oplus$ of the inner planet, implying its density 10^4 times smaller than the density of the Earth.

The mass estimates in the TTV model in Tab. 1 have small uncertainties of $\simeq 20\%$. Their values are consistent with predictions from the mass–radius relation $M = 10^C \times R^E$, where $C = 0.50 \pm 0.03$ and $E = 0.64 \pm 0.06$ (Mills & Mazeh 2017).

Having the relatively accurate mass and radii estimates, we may infer the densities of the two planets. Given the similar radii and the inner planet twice as massive as the outer one, the internal compositions of the planets are likely different. We used two-layer theoretical models by Zeng et al. (2016) in order to localise the planets in the mass-radius diagram in Fig. 4.

Two internal composition models were obtained. For the MCMC-model with $\Delta\varpi = \pi$ (Tab. 1), the inner planet has a bulk density of (7.1 ± 0.3) g·cm^{-3}, roughly 1.5 density of the Earth. The density of the second planet is (3.6 ± 0.3) g·cm^{-3}, roughly the density of Mars (i.e. 3.9 g·cm^{-3}). For dual-mode solutions ($\Delta\varpi = \pi, 0$), the masses (Fig. 2) as well as the derived densities are significantly smaller, (5.6 ± 0.5) g·cm^{-3} and (2.9 ± 0.6) g·cm^{-3}, respectively.

Both classes of the internal structure models predict the inner planet as a Super-Earth with a rocky envelope and a small iron-rich core. The outer planet is found in the region between rocky and icy-giant planets, populated by a new class of objects. They are called "Super-Venus" planets (e.g., Kane et al. 2013) if they are, as KOI-1599.02, close to the host star.

7 CONCLUSIONS

With the dynamical photometry, we aim to validate two transiting, candidate planets attributed to the KOI-1599 KEPLER target.

From the Q1-Q17 DR-25 LCs, we derived complete series of TTVs with a few hours amplitude. They exhibit a clear anti-correlation trend, indicating that the candidate planets mutually interact. Dynamical experiments make it possible to determine the upper limits of the candidate masses, below roughly 3 Jupiter masses that provide dynamically stable configurations. The photometric analysis of the LCs of KOI-1599 reveals that the planets have very similar radii, $\simeq 1.9$ times of the Earth's radius.

The orbital model of the TTVs makes it possible to constrain the masses in the Super-Earth range of 9.0M$_\oplus$ and 4.6M$_\oplus$, for the inner and the outer planet, respectively. The uncertainties may be as small as $\simeq 20\%$. However, we assumed that the orbits are low-eccentric ($e_i \simeq 0.01$) and anti-aligned, consistent with predictions of the planetary migration theory (e.g., Batygin & Morbidelli 2013). Given the similar radii, the internal compositions of the planets may be different.

Remarkably, independent on eccentricities and $\Delta\varpi = \pi, 0$ libration modes, the best-fitting orbital models are dynamically "easily" involved in the 3:2 MMR. Dynamical maps reveal that the best-fitting configurations are inside the separatrix region of the 3:2 MMR, although the critical angles can circulate or librate with amplitudes reaching 2π (so only are coherent). The apparently natural libration–circulation criterion of the critical angles may lead to an incorrect identification of the MMR.

The results of our statistical and dynamical experiments are suggestive of two real planets. Given a limited span of the photometry, additional experiments in the framework of refined migration theory, beyond simple models computed in this work, may better constrain the eccentricities and masses of the planets.

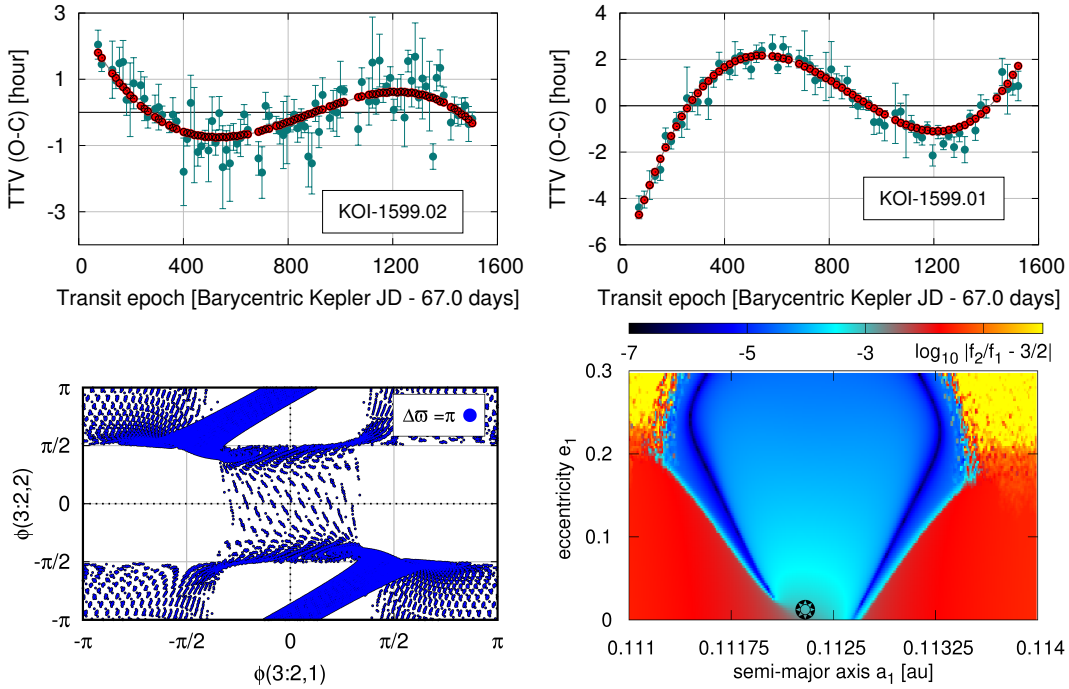

Figure 3. *Upper row*: Synthetic TTV signals and the measurements, for a representative MCMC solution with anti-aligned apsides (see Tab. 1). This model yields $\chi^2_\nu \simeq 1.1$. *Bottom row*: Evolution of the critical angles, and a dynamical map in terms of the proper mean motions f_1, f_2 ratio, relative to the 3:2 MMR. The star marks the model initial condition varied across the grid (300×100 points) and integrated for 1048576 time-steps of 0.4 d to resolve $f_{1,2}$.

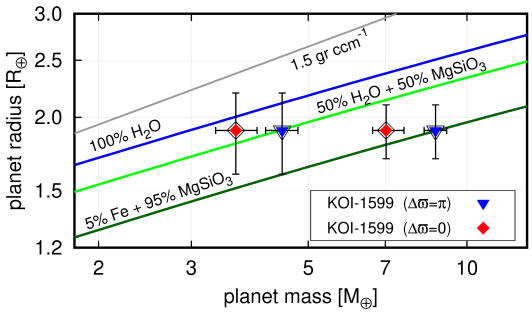

Figure 4. The mass-radius diagram for mass estimates in two $\Delta\varpi = \pi$ (blue squares) and $\Delta\varpi = \pi, 0$ (red triangles) orbital modes.

8 ACKNOWLEDGEMENTS

K. G. thanks the staff of the Poznań Supercomputer and Network Centre (PCSS) for the support and CPU resources (grant No. 313). This work has been supported by Polish National Science Centre MAESTRO grant DEC-2012/06/A/ST9/00276.

REFERENCES

Agol E., et al. 2005, MNRAS, 359, 567
Baranec C., et al. 2016, AJ, 152, 18
Batygin K., Morbidelli A., 2013, AJ, 145, 1
Borucki W. J., et al. 2011, ApJ, 728, 117
Carter J. A., et al. 2012, Science, 337, 556
Cincotta P. M., Simó C., 2000, A&AS, 147, 205
Deck K. M., Agol E., 2015, ApJ, 802, 116
Delisle J.-B., Laskar J., 2014, A&A, 570, L7
Espinoza N., et al. 2016, ApJ, 830, 43
Fabrycky D. C., et al. 2014, ApJ, 790, 146
Foreman-Mackey D., et al. 2013, PASP, 125, 306
Goldreich P., Schlichting H. E., 2014, AJ, 147, 32
Goździewski K., Breiter S., Borczyk W., 2008, MNRAS, 383, 989
Goździewski K., et al. 2016, MNRAS, 455, L104
Hadden S., Lithwick Y., 2014, ApJ, 787, 80
Henrard J., Lamaitre A., 1983, Celestial Mechanics, 30, 197
Holczer T., et al. 2016, AJSS, 225, 9
Holman M. J., et al. 2010, Science, 330, 51
Jontof-Hutter D., et al. 2016, ApJ, 820, 39
Kane S. R., Barclay T., Gelino D. M., 2013, ApJL, 770, L20
Kovács G., Zucker S., Mazeh T., 2002, A&A, 391, 369
Lee M. H., Peale S. J., 2002, ApJ, 567, 596
Lissauer J. J., et al. 2011, ApJS, 197, 8
Lithwick Y., Wu Y., 2012, ApJL, 756, L11
MacDonald M. G., et al. 2016, AJ, 152, 105
Migaszewski C., Goździewski K., 2018, MNRAS, 480, 1767
Mills S. M., Mazeh T., 2017, ApJL, 839, L8
Nesvorný D., et al. 2013, ApJ, 777, 3
Panichi F., et al. 2018, MNRAS
Papaloizou J. C. B., 2015, Int. Journal of Astrobiology, 14, 291
Papaloizou J. C. B., Larwood J. D., 2000, MNRAS, 315, 823
Press W. H., Flannery B. P., Teukolsky S. A., 1986, Numerical recipes. The art of scientific computing. Cambridge Univ. Press
Rowe J. F., et al. 2014, ApJ, 784, 45
Rowe J. F., et al. 2015, ApJS, 217, 16
Šidlichovský M., Nesvorný D., 1996, CMDA, 65, 137
Spiegel D. S., Burrows A., Milsom J. A., 2011, ApJ, 727, 57
Steffen J. H., et al. 2012, MNRAS, 421, 2342
Steffen J. H., Hwang J. A., 2015, MNRAS, 448, 1956
Weiss L. M., et al. 2016, ApJ, 819, 83
Zeng L., Sasselov D. D., Jacobsen S. B., 2016, ApJ, 819, 127